Heliyon 9 (2023) e22319

Contents lists available at ScienceDirect

Heliyon

journal homepage: www.cell.com/heliyon

Magnetite nanoparticles decorated on cellulose aerogel for *p*-nitrophenol Fenton degradation: Effects of the active phase loading, cross-linker agent and preparation method

Thi Thuy Van Nguyen [a,b,1], Quang Khai Nguyen [c,d], Ngoc Quan Thieu [c,d], Hoang Diem Trinh Nguyen [c,d,1], Thanh Gia Thien Ho [a], Ba Long Do [a], Thi Thuy Phuong Pham [a,b], Tri Nguyen [a,b,**], Huynh Ky Phuong Ha [c,d,*]

[a] *Institute of Chemical Technology, Vietnam Academy of Science and Technology, No.1A, TL29 Str., Thanh Loc Ward, Dist. 12, Ho Chi Minh City, Viet Nam*
[b] *Graduate University of Science and Technology, Vietnam Academy of Science and Technology, 18 Hoang Quoc Viet Street, Cau Giay District, Hanoi, Viet Nam*
[c] *Ho Chi Minh City University of Technology (HCMUT), 268 Ly Thuong Kiet Str., Dist. 10, Ho Chi Minh City, Viet Nam*
[d] *Vietnam National University Ho Chi Minh City, Linh Trung Ward, Thu Duc Dist., Ho Chi Minh City, Viet Nam*

ARTICLE INFO

Keywords:
Cellulose aerogel
Magnetite nanoparticle
P-nitrophenol
Fenton degradation
Cross-linker

ABSTRACT

Magnetite nanoparticles (Fe_3O_4 NPs) are among the most effective Fenton-Like heterogeneous catalysts for degrading environmental contaminants. However, Fe_3O_4 NPs aggregate easily and have poor dispersion stability because of their magnetic properties, which seriously decrease their catalytic efficiency. In this study, a novel environmentally friendly method for synthesising Fe_3O_4@CA was proposed. Fe_3O_4 NPs were immobilized on the 3D cellulose aerogels (CAs) in order to augment the degradation efficiency of *p*-nitrophenol (PNP) treatment and make the separation of the catalyst accessible by vacuum filtration method. Besides, CAs were fabricated from a cellulose source extracted from water hyacinth by using different cross-linking agents, such as kymene (KM) and polyvinyl alcohol–glutaraldehyde system (PVA–GA), and other drying methods, including vacuum thermal drying and freeze drying, were evaluated in the synthesis process. As-synthesized samples were analysed by various methods, including Powder X-ray diffraction, Fourier transform infrared spectroscopy, field emission scanning electron microscopy, energy dispersive X-ray analysis and Brunauer–Emmett–Teller. Then, using ultraviolet–visible spectroscopy, the difference in the degradability of PNP of the obtained material samples was also investigated to determine their potential applications. Results highlighted that the Fe_3O_4-3@CA-KF catalyst with an Fe_3O_4 loading of 0.40 g/g_{CA} used KM as a cross-linker and the freeze-drying method demonstrated the highest PNP removal efficiency (92.5 %) in all Fe_3O_4@CA samples with a H_2O_2 content of 5 g/L. The degradation kinetics and well-fitted pseudo-first-order model were investigated. Notably, after five successive PNP degradation experiments, this catalyst retained ~80 % of the ability to degrade PNP, indicating its outstanding reusability. In environmental

* Corresponding author.Ho Chi Minh City University of Technology (HCMUT), 268 Ly Thuong Kiet Str., Dist. 10, Ho Chi Minh City, Viet Nam.
** Corresponding author.Institute of Chemical Technology, Vietnam Academy of Science and Technology, No.1A, TL29 Str., Thanh Loc Ward, Dist. 12, Ho Chi Minh City, Viet Nam.
E-mail addresses: ntri@ict.vast.vn (T. Nguyen), hkpha@hcmut.edu.vn (H. Ky Phuong Ha).
[1] Those authors contributed equally.

https://doi.org/10.1016/j.heliyon.2023.e22319
Received 9 June 2023; Received in revised form 6 November 2023; Accepted 9 November 2023
Available online 14 November 2023

remediation, this study provides valuable insights into the development of simply separated and high-efficiency catalysts for heterogeneous catalytic reactions.

1. Introduction

Aerogels have attracted significant attention due to their notable characteristics, including their high porosity, low density, porous structure, huge specific surface areas, and very low thermal conductivity [1,2]. Because of their abundant availability, renewable natural resources and favourable biodegradability, cellulose-based aerogels have garnered significant attention and used in several sectors, such as food [3], energy storage [4], wastewater treatment [5,6], wound dressing [7] and pharmaceutical industries [8] over the last decades. Cellulose aerogel from water hyacinth has been fabricated and published in many previous works [9–11]. It has a variety of uses and possesses numerous unique properties, such as extremely low density (0.003–0.500 g/cm^3), high porosity (80 %–99.8 %), huge surface area (100−1600 m^2/g) and high compressive strength (5.20 kPa–16.67 MPa) and has good surface activity.

The aerogels' three-dimensional networks, characterized by several open cavities, enable efficient molecular or ionic transportation, rendering them highly appropriate for developing functional materials that serve as exceptional support for various nanoparticles (NPs) [12,13]. Numerous research has been conducted to investigate the development of composite materials using functional matrices for the fabricating of organic or inorganic hybrid composites, including various constituents, such as SiO_2 [14], TiO_2 [15], $CoFe_2O_4$ [16] and $CaCO_3$ [17]. These composite materials have demonstrated prospective applications in the fields of life science, environment, and catalysis, rendering them the most promising. However, studies that have modified metallic NP catalysts on CA to create heterogeneous catalyst systems for environmental treatment applications are rare. Moreover, CA materials from water hyacinth with suitable cross-linkers and optimal synthesis conditions have high potential as materials that enable catalysts to decompose difficult organic pollutants, such as *p*-nitrophenol (PNP) with high concentrations.

However, the matrix of native CAs is often stiff and rapidly collapses when soaked in water, restricting their scope of applicability [18,19]. Improving their mechanical strength and water stability is tough. Some researchers have mixed cellulose with kymene [10,20], used a combination of polyvinyl alcohol (PVA) and glutaraldehyde [10,21] and a cross-linking agent to solve the aforementioned deficiency in the performance of cellulose. Different cross-linkers alter the characteristics of CA, thus affecting their usefulness as catalyst carriers and the activity of the catalytic system [22]. Therefore, investigating the influence of cross-linking agents on catalytic activity during CA synthesis is crucial. Drying procedures used in CA synthesis, such as heat drying or sublimation drying, have substantial impacts on a product's characteristics [23]. CA's porosity, density, mechanical strength and reform ability are dependent on the drying procedure. No published findings have indicated that drying conditions alter catalytic activity, stability or reusability of CA in catalyst systems.

Numerous studies have utilized the heterogeneous Fenton procedure to handle PNP in wastewater [24–27]. By generating *OH radicals with potent oxidizing activity, these radicals are intended to facilitate the decomposition of organic compounds utilizing Fe_3O_4 catalysts [28,29]. The Fe_3O_4 nanoparticles have attracted significant attention due to their large specific surface area, superparamagnetic properties, biocompatibility, catalytic activity, and environmentally favourable characteristics [2]. Nevertheless, these nanoparticles are prone to aggregation and the subsequent production of larger particles, resulting in a decrease in their overall activity [30]. Consequently, the incorporation of a carrier is required to immobilize Fe_3O_4 NPs.

Herein, a straightforward and ecofriendly approach for decorating CAs with Fe_3O_4 with different synthesis methods was established, and PNP degradation performance was evaluated. Simultaneously, the findings demonstrated that CA is an exceptional matrix for supporting Fe_3O_4 NPs. Besides, Fe_3O_4 modified on a CA surface (Fe_3O_4@CA) was produced from water hyacinth. For the cross-linking agent, the method employed kymene and the PVA-GA system. In addition, heat drying, and sublimation drying were used in Fe_3O_4@CA synthesis. We examined the physicochemical features of the catalyst system, and PNP degradation, recovery and reuse, to validate the product's prospective applicability.

2. Methodology

2.1. Chemicals and reagents

Water hyacinth was gathered from Sai Gon River in Ho Chi Minh City's District 12. Ferric chloride ($FeCl_3.6H_2O$, Xilong, 99 %) and ferrous sulphate ($FeSO_4.7H_2O$, Xilong, 99 %) were used in the preparation of Fe_3O_4 NPs. Kymene (Solenis 5574), glutaraldehyde (25 % in H_2O, Aldrich) and PVA (M_n ~145.000) were used as cross-linking agent. Sodium hydroxide (NaOH, Xilong, 99 %), hydrogen peroxide (H_2O_2, Xilong, 30 %), sulphuric acid (H_2SO_4, Xilong, 95 %), sodium chlorite ($NaClO_2$, 80−83 %) and PNP (Tianjin Chemical Reagent 99 %). All of the reagents used in the experiment were employed without undergoing purification. All studies used water that has been filtered using a Milli-Q system.

2.2. Synthesis of samples

2.2.1. The process of extracting cellulose from water hyacinth

A combination was created by blending 2 % w/w dried WH fibres with a 2 % w/w NaOH solution for lignin and hemicellulose removal. The removal efficiency was enhanced by subjecting the combination to microwave heating for a duration of 20 min using the

AEM-G2135W microwave model manufactured by AQUA. An aqueous solution of H_2O_2 with a concentration of 17 % (v/v) was introduced into the microwave-treated mixture after it had been cooled. The pH of the combination was then approximately adjusted to 11 using NaOH before subjecting the mixture to an additional 10 min of microwave heating. Following the cooling of the combination to ambient temperature, it underwent filtration and subsequent rinsing with distilled water in order to get a pH value of 7.0. The pre-treated material underwent a drying process at a temperature of 70 °C for 24 h, after which it was then kept for the purpose of aerogel manufacturing [9].

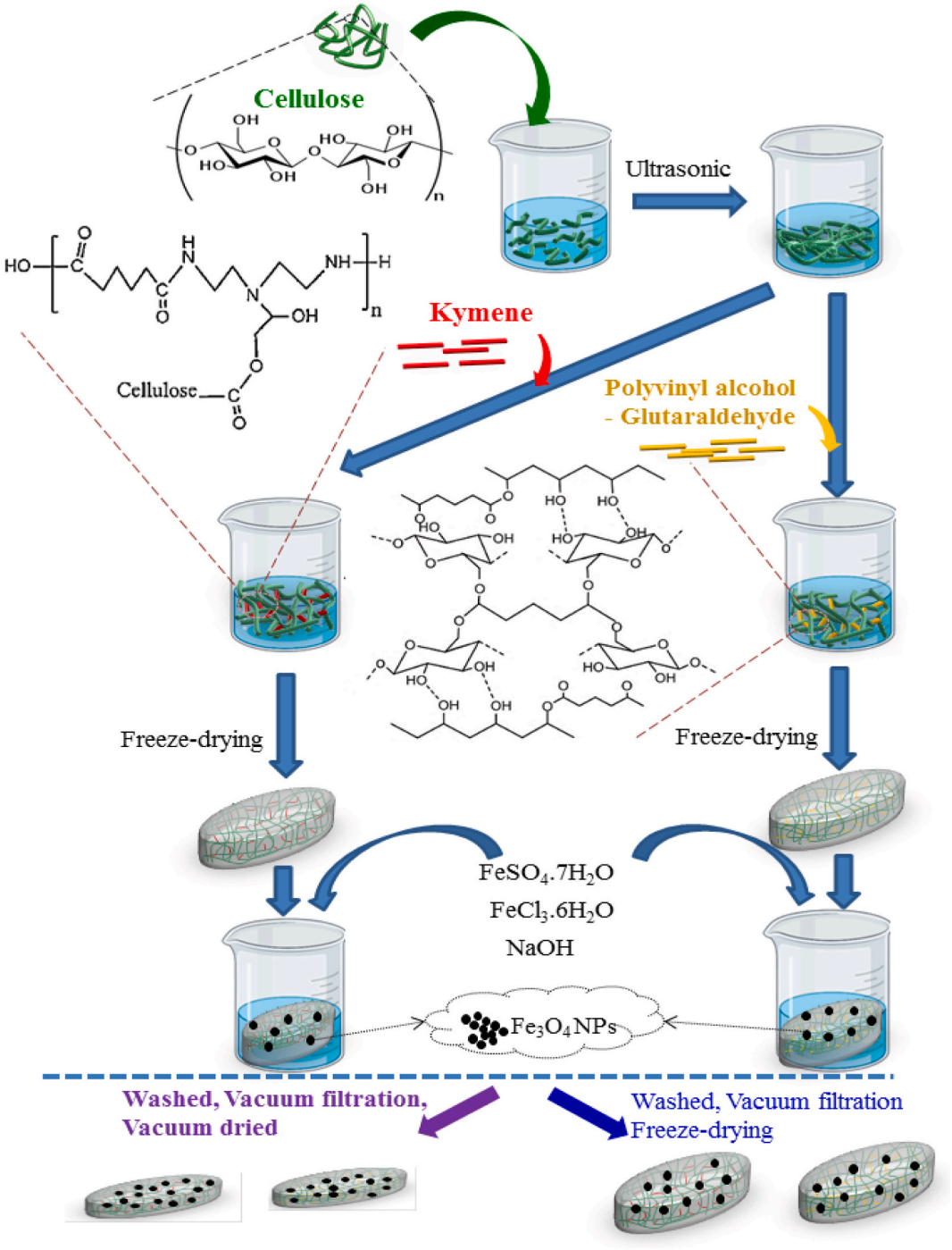

Fig. 1. A schematic representation of the experimental technique of manufacture of Fe_3O_4 NPs decorated on CA.

2.2.2. Preparation of Fe_3O_4@CA-K using kymene as the cross-linker

CA samples (CA-K) were prepared as previously reported [7,8]. A homogeneous mixture was prepared by mixing 100 mL of a cellulose fiber solution with a concentration of 2 % w/w in water. Subsequently, a volume of 0.5 mL of kymene was introduced into the mixture and agitated for 2 h using a magnetic stirrer operating at a speed of 800 revolutions per minute. The combination was subjected to refrigeration for a duration of 24 h prior to undergoing sublimation at a temperature of −70 °C, resulting in the acquisition of an aerogel sample. Subsequently, the acquired components were subjected to an oven at a temperature of 80 °C for a duration of 3 h, with the purpose of augmenting the cross-linking of kymene inside the resultant aerogel cellulose product [10].

The fabrication process of the Fe_3O_4@CA-K samples involved the coprecipitation method. Firstly, 1.6 g of CA-K was dispersed in a mixture of 100 mL containing an aqueous solution of $FeSO_4.7H_2O$ and $FeCl_3.6H_2O$ in a 1:1 M ratio. Proceeding to agitate while maintaining the inert medium for the reaction at 75 ± 5 °C, 200 mL of distilled water was subsequently added to the mixture in a 500 mL beaker equipped with a magnetic agitator. The reaction was continued for an additional 40 min after the pH was adjusted to 11.5 with a 1 M NaOH solution. The acquired substance was rinsed with ethanol and distilled water until pH 7 was reached. The sample was dried with two methods: i) vacuum drying for 12 h at 60 °C to obtain Fe_3O_4-X@CA-KV (*X* was varied [1–4] corresponding to the content of Fe_3O_4 in samples [0.17, 0.25, 0.40 and 0.49 g/g_{CA}, respectively]; Table S1) and ii) freeze drying within 24 h to obtain Fe_3O_4-X@CA-KF.

2.2.3. Preparation of Fe_3O_4@CA-P by using PVA and GA as the cross-linker

CA samples (CA-P) were generated in the identical manner as CA-K. A PVA (5 % w/w in water) solution was introduced to 100 mL of a 2 % (w/w in water) cellulose fiber combination at a PVA-to-cellulose ratio of 4:3. After incorporating 0.1 mL of 1 % H_2SO_4 and 0.25 mL of GA (25 % w/w in water), the mixture was agitated for an additional 1 h at 800 rpm using a magnetic stirrer. CA-P was obtained through the freeze-drying process of cellulose hydrogel at −70 °C for 24 h. To enhance the PVA-GA's cross-linking, the aerogel material was cured for an additional 3 h at 80 °C [10].

Method of synthesising Fe_3O_4@CA-P via coprecipitation: 1.6 g of CA-P was immersed in 100 mL of an aqueous $FeSO_4.7H_2O$ and $FeCl_3.6H_2O$ solution. The best ratio and molar number were selected according to the previous experiments of Fe_3O_4-*x*@CA-K. Then, a volume of 200 mL of distilled water was introduced into a 500 mL beaker with a magnetic stirrer, keeping the reaction's inert medium at 75 ± 5 °C. The sample was dried with two methods: i) vacuum drying for 12 h at 60 °C to obtain Fe_3O_4-X@CA-PV; ii) freeze-dried within 24 h to obtain Fe_3O_4-X@CA-PF. The fabrication of the synthesis of magnetite NPs decorated on CA is illustrated in Fig. 1.

2.3. Characterisation

The crystal structure of pure CA and Fe_3O_4@CA catalysts were examined using X-ray diffraction (XRD, D2-PHASER) with Cu Kα radiation and recorded at 2θ = 10°–80° and Fourier transform infrared (FTIR) system (Tensor 27 Bruker Instrument) at a range of 400–4000 cm^{-1}. A scanning electron microscope (Hitachi, S-4800) and high-resolution transmission electron microscopy (JEOL JEM 1400 equipment) were utilized in observing surface morphology, pore structure and Fe_3O_4 particles on the surfaces of the materials. Additionally, the composition of the catalyst materials was evaluated, and energy-dispersive X-ray spectroscopy was employed to analyze the elemental distribution on the surfaces of the catalysts (EDS, JEOL JST-IT 200).

The experimental procedure for synthesising Fe_3O_4 NPs that are decorated on CA is depicted in the schematic. The Nova Station A was utilized to conduct nitrogen physical adsorption measurements, and Quantachrome was employed to estimate the surface area, pore size, and pore volume of the materials. The Brunauer–Emmett–Teller (BET) equation and Barret–Joyner–Halenda (BJH) techniques were used to automatically derive these parameters from the equipment software. The point of zero charge (PZC) of the samples was determined with the salt addition technique through previously described method [31]. The magnetic characteristics of the Fe_3O_4@CA composites were examined at room temperature with a vibrating sample magnetometer (VSM) across a field range spanning from −11,000 to +11,000 Oe (ADE Technology–DMS 5000).

2.4. Fenton-like degradation experiments

The PNP solution (2000 ppm) utilized in the experiment comprised of 500 mL distilled water and 1.00 g of PNP. The initial pH of the procedure was adjusted to 3 by adding a 95 % H_2SO_4 solution. H_2O_2 was added to the solutions along with Fe_3O_4@CA-K and Fe_3O_4@CA-P samples. Samples were collected at 20-min intervals throughout the reaction, and the degradation of PNP was observed using ultraviolet–visible (UV–Vis) spectroscopy. The spectrum of wavelengths was recorded in the range of 190–800 nm, and the total reaction time was 180 min. The maximum absorption in the spectrum was detected at a wavelength of 317 nm. The removal of PNP was determined by employing Equation (1).

$$H\% = \frac{(C_0 - C_t)}{C_0} \times 100\%, \quad (1)$$

Where, the variables C_0 and C_t represent the concentrations of PNP at the initial time (0) and at an additional point (t) during the reaction, respectively.

2.5. Recyclability measurements

In assessing the practical application potential of catalysts, reusability is one of the essential characteristics. The recyclability of the optimal catalyst for degrading PNP via heterogeneous Fenton was tested under optimised reaction conditions for five cycles. After each degrading cycle, Fe_3O_4-3@CA-KF was removed from the solution through vacuum filtering for reusability testing, and the supernatant was collected. The filtered Fe_3O_4-3@CA-KF was then rinsed with deionised water to eliminate contaminants before it was employed in the subsequent degradation experiment. The degradation rates of PNP solutions and their accompanying UV–Vis absorption spectra were determined.

3. Results and discussion

3.1. Catalytic activity

3.1.1. Effect of Fe_3O_4 loading

In a Fenton-like system, PNP was chosen as the model organic pollutant to assess the catalytic activity of Fe_3O_4@CA-KV. The pH value plays a crucial role in the Fenton process because it governs the generation of hydroxyl radicals [32]. The literature reports that an acidic pH is useful in removing pollutants because H_2O_2 has high stability at low pH levels and does not dissociate into O_2 and H_2O [33]. Based on prior research, the investigation of the Fenton decomposition process has shown that a pH level of 3 is considered to be the most [34–36]. Therefore, for the purpose of this investigation, a fixed pH value of 3 was used in the examination of additional variables in the degrading response of PNP.

The PNP degradation process was carried out on Fe_3O_4@CA-KV samples containing different amounts of Fe_3O_4. The initial solution pH was set at 3 and the H_2O_2 concentration was set at 4.0 g/L. The stirring speed during the process was 300 rpm. Fig. 2 depicts the process of eliminating PNP from a solution using an initial concentration of 2000 ppm, following a reaction time of 180 min. The results showed that all the samples can be used to degrade PNP and showed different levels of efficiency. After 100 min of reaction, the PNP conversion efficiency were 57.6 % for Fe_3O_4-1@CA-KV, 79.1 % for Fe_3O_4-2@CA-KV, 85.5 % for Fe_3O_4-3@CA-KV and 86.2 % for Fe_3O_4-4@CA-KV. When the Fe_3O_4 content was increased, the reaction rate increased significantly because the introduction of Fe_3O_4 NPs might have increased the number of active sites for *OH production. However, increase in the Fe_3O_4 content in Fe_3O_4-3@CA-KV and Fe_3O_4-4@CA-KV promoted PNP conversion but not significantly. After 100 min of reaction, the conversion yields of Fe_3O_4-3@CA-KV and Fe_3O_4-4@CA-KV were practically stable. At low concentrations, the inefficiency of Fe^{3+} removal was attributable to the low level of *OH radical formation required for oxidation. Conversely, the surplus Fe^{3+} ions effectively eliminated the formed *OH, thereby potentially impeding the degradation of PNP [37]. Thus, the Fe_3O_4-3@CA-KV sample with 0.40 g/g_{CA} of Fe_3O_4 achieved the highest PNP conversion efficiency, although Fe_3O_4-4@CA-KV had the highest amount of loaded Fe_3O_4 NPs (0.49 g/g_{CA}). This result indicated that the PNP degradation efficiency is not proportional to the loaded amount of Fe_3O_4 at high content. The findings were consistent with the existing literature, which posited that the degradation rate of organic pollutants rises in proportion to the concentration of Fe_3O_4, up to a certain threshold beyond which additional Fe_3O_4 incorporation has minimal impact [38]. Thus, Fe_3O_4-3@CA-KV was selected for all subsequent experiments.

3.1.2. Effect of H_2O_2 dosage

The presence of iron plays a critical role in the function of H_2O_2 as an oxidizing agent. To augment the competitiveness of the Fenton process in comparison to alternative processes, it is crucial for the applications to demonstrate a cost-effective operation, as well as enhanced control over the dosage of H_2O_2. The primary aim of the experiment was to optimize the Fenton degradation process

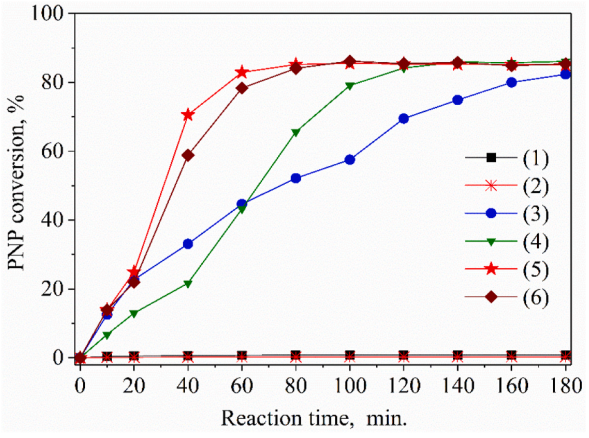

Fig. 2. The investigation of the activity of samples in the heterogeneous Fenton degradation of PNP; 1) PNP + H_2O_2; 2) PNP + Fe_3O_4-1@CA-KV; 3) PNP + H_2O_2 + Fe_3O_4-1@CA-KV, 4) PNP + H_2O_2 + Fe_3O_4-2@CA-KV; 5) PNP + H_2O_2 + Fe_3O_4-3@CA-KV; 6) PNP + H_2O_2 + Fe_3O_4-4@CA-KV.

to attain optimal performance levels, while simultaneously minimizing the consumption of H_2O_2. The effects of H_2O_2 content on Fe_3O_4-3@CA-KV are shown in Fig. 3. H_2O_2 concentration had a substantial influence on PNP elimination over time. After 80 min, the elimination effectiveness of PNP with varying H_2O_2 dosages was almost stable. When the dosage of H_2O_2 was raised from 3 g/L to 5 g/L, the conversion efficiency of PNP significantly increased from 77.1 % to 92.0 %. The experimental results suggested that when the concentration of Fe_3O_4 had a specified value, raising the H_2O_2 dosage caused the production of •OH radicals, which considerably enhanced the oxidation rate and degree of mineralisation [39].

The further enhancement from 5 g/L to 6 g/L initiated no notable change in PNP degradation. After 80 min of reaction, the PNP conversion efficiency reached 85.5 % with 6 g/L of H_2O_2 and 92 % with 5 g/L of H_2O_2. This result can be explained by the high H_2O_2 dosage, at which *OH is scavenged. The aforementioned phenomenon led to the generation of hydroxyl radicals, which exhibit lower reactivity compared to *OH and consequently impeded the conversion of PNP [40].

Under acidic conditions, the activation of H_2O_2 proceeds through a process wherein a complex of ≡ FeIII and H_2O_2 forms [24,41,42]. This complex is denoted as ≡ $FeIIIH_2O_2$ (Eq. (2)), where ≡ FeIII represents Fe(III) sites present on the surface of a catalyst. The first formed ≡ $FeIIIH_2O_2$ species undergo a conversion to ≡ FeII species and $*HO_2$ (Eq. (3)). Additionally, the created $*HO_2$ may react further with ≡ FeIII to yield ≡ FeII species (Eq. (4)). The various ≡ FeII species (Eq. (5)) can undergo a reaction with H_2O_2, resulting in the production of *OH radicals. These radicals are extremely effective in degrading and mineralising PNP (Eq. (6)). This process aligns with the findings in the literature, which have demonstrated the ability of iron oxide to catalyse the activation of H_2O_2 and to promote the generation of *OH radicals.

$$\equiv FeIII + H_2O_2 \rightarrow \equiv FeIIIH_2O_2 \quad (2)$$

$$\equiv FeIIIH_2O_2 \rightarrow \equiv FeII + *O_2H + H^+ \quad (3)$$

$$\equiv FeIII + *O_2H \rightarrow \equiv FeII + O_2 + H^+ \quad (4)$$

$$\equiv FeII + H_2O_2 \rightarrow \equiv FeIII + *OH + OH^- \quad (5)$$

$$*OH + PNP \rightarrow \text{low molecular substances} + CO_2 + H_2O \quad (6)$$

3.1.3. *Effects of cross linkers and drying methods*

The effects of different cross-linkers and drying methods on PNP conversion efficiency were investigated (Fig. 4). The results showed that the degradation performance of PNP was reduced in the order Fe_3O_4-3@CA-KF > Fe_3O_4-3@CA-PF > Fe_3O_4-3@CA-KV > Fe_3O_4-3@CA-PV (Fig. 4a). CA samples using kymene as a cross-linker had significantly better PNP degradation efficiency. The aforementioned outcome has been elucidated in a prior investigation [8], wherein it was demonstrated that kymene exhibits aptitude as a cross-linking agent due to its ability to form cross-links via its epichlorohydrin moieties. The presence of cross-links improves the interaction between kymene and cellulose, thereby improving the mechanical strength, especially in wet conditions, of aerogels. PVA and GA can promote the formation of three-dimensional interconnected continuous network in a matrix material through hydrogen bonding and facilitate aerogel synthesis through PVA and GA cross-linking. Nevertheless, the products exhibit limited mechanical strength and lack high compressibility. Consequently, the CA samples incorporating kymene as a cross-linker exhibit greater porosity and reduced density compared to the samples utilizing PVA and GA as cross-linkers as cross-linkers. Moreover, the specific surface areas of heterogeneous catalysts were identified as the most significant parameter affecting the degradation activity of PNP [43,44]. As the specific surface area of a catalyst increases, the sites where degradation reactions occur can be increased.

Fig. 4 shows that the freeze-drying method has a higher degradation efficiency for PNP than the vacuum-drying method. The

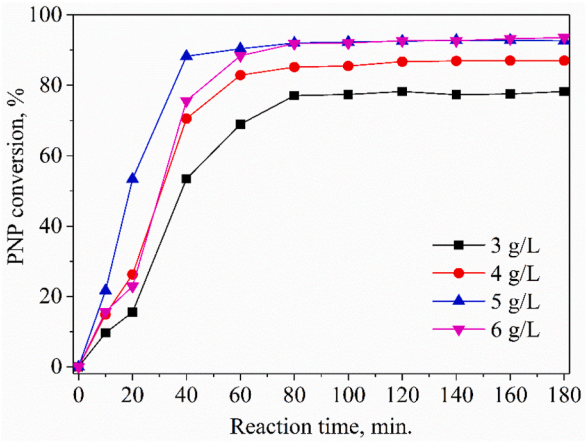

Fig. 3. The impact of H_2O_2 dosage on the heterogeneous Fenton degradation of PNP occurring on a catalyst composed of Fe_3O_4-3@CA-KV.

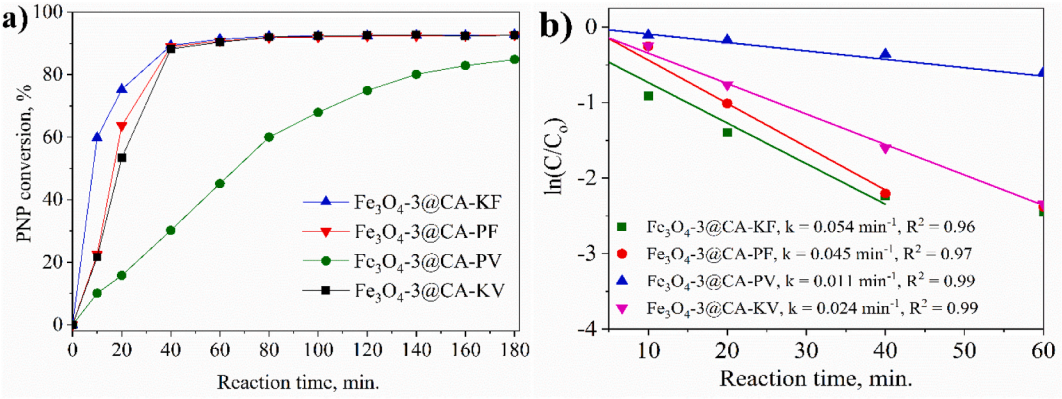

Fig. 4. Effects of cross-linkers and drying methods on the heterogeneous Fenton degradation of PNP.

freeze-drying samples of CA had higher porosity and lower densities than the samples obtained through vacuum drying. These results can be explained by the low pressure and low water evaporation temperature in vacuum drying, which can cause the pores to shrink or collapse. The resulting samples would have low porosity and specific surface area. Meanwhile, freeze drying can create a sheet-like cellulose network with large and interconnected pores of a few micrometers in diameter because pore sites were frozen before vaporisation creates new pores, resulting in products with high porosity and large specific surface areas [45].

The effects of cross-linkers and drying methods on the degradation kinetics curves of PNP were determined. The compatibility between the collected data and the pseudo-first kinetic model was assessed through experimentation. The model can be expressed as Eq. (7):

$$ln\left(\frac{C_t}{C_0}\right) = -k_1 t, \tag{7}$$

where C_0 is the initial concentration of PNP and C_t is the concentration at time t. Given that all R^2 values exceeded 0.95, it can be concluded that this model is highly appropriate for the specific reaction under consideration. The reaction rate constants of Fe_3O_4-3@CA-KF, Fe_3O_4-3@CA-PF, Fe_3O_4-3@CA-KV and Fe_3O_4-3@CA-PV were 0.054, 0.045, 0.024 and 0.011 min^{-1}, respectively, after linear fitting (Fig. 4b). These results were in close agreement with previous research [46,47]. The reaction rate constants were estimated, and the highest rate was found in Fe_3O_4-3@CA-KF.

3.2. Material characterisation

The XRD patterns of the Fe_3O_4@CA samples (Fig. 5a) exhibit characteristic peaks at specific angles, namely $2\theta = 30.88°$, 36.09°, 43.86°, 53.64°, 57.79°, and 63.43°. These peaks correspond to the diffraction lattice surfaces (220), (311), (400), (422), (511), and (440), respectively, as indicated by the JCPDS card 01-075-0449. These findings align with previous studies on the subject matter [48,49]. In addition, the observed peaks at $2\theta = 16.51°$ and 23.14°, which correspond to the diffraction lattice surfaces (110) and (200) respectively, are indicative of the distinctive peaks associated with crystalline cellulose [50]. The obtained results have substantiated the existence of Fe_3O_4 crystals within the CA structure. The intensity of the cellulose diffraction peaks in the Fe_3O_4@CA samples was noticeably lower compared to those of the pure CA samples. This suggests a decrease in the degree of crystallinity and suggests that

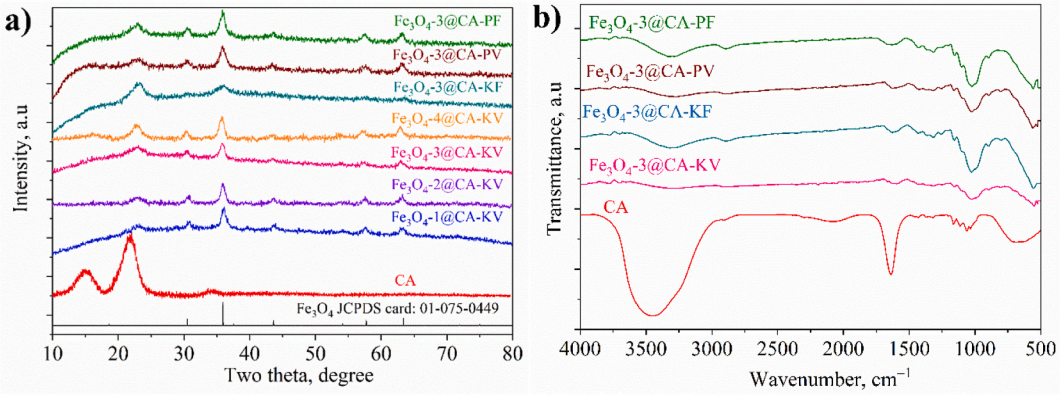

Fig. 5. XRD patterns (a) and FTIR spectra (b) of samples.

there was some form of interaction between the CA and Fe_3O_4 NPs. These interactions likely influenced the crystallization process of cellulose within the Fe_3O_4-decorated aerogels.

The average crystallite size of each sample was determined by using the Scherrer equation [51] at characteristic peak (2θ) of 36.09°. Hence, the average crystallite sizes of Fe_3O_4 NPs in Fe_3O_4-1@CA-KV, Fe_3O_4-2@CA-KV, Fe_3O_4-3@CA-KV, Fe_3O_4-4@CA-KV, Fe_3O_4-3@CA-KF, Fe_3O_4-3@CA-PV and Fe_3O_4-3@CA-PF were 6.5, 6.9, 7.4, 7.7, 7.1, 7.6 and 7.4 nm, respectively. When the Fe_3O_4 content increased, the average crystallite size increased with the same drying method. At the same content, the average crystallite size of Fe_3O_4 did not change significantly. These results can be explained by the agglomeration of Fe_3O_4 on the surface of the CA samples.

In order to determine the functional group of the CA and Fe_3O_4@CA samples, an FTIR analysis was conducted within the absorption region of 4000−400 cm^{-1} (Fig. 5b). All samples exhibited consistent absorption peaks at 2900, 1625, 894 and 554 cm^{-1}, although their intensities displayed variation. This observation suggests an interaction between Fe_3O_4 nanoparticles and cellulose molecules. Furthermore, the introduction of Fe_3O_4 NPs led to the association of oxygen atoms with the OH and COOH groups. This association resulted in the expansion of the O–H stretching peak and a shift from 3425 cm^{-1} (pure CA) to 3320 cm^{-1} (Fe_3O_4@CA sample). In particular, anionic groups have the ability to establish coordination-type interactions with metal ions, thereby promoting the creation of ultrafine nanoparticles that exhibit a remarkably dispersion on the surface of the CA material [52]. The peak observed at 554 cm^{-1} was found to correspond to the vibration of the Fe–O functional group. This vibration exhibited a strong similarity to the characteristic peak of Fe_3O_4, as reported in previous studies [53,54]. The observed peak at 2900 cm^{-1} can be attributed to the vibrational mode of the –CH group in cellulose, while the peak at 1605 cm^{-1} corresponds to the bending vibration of the –OH group in water that is naturally

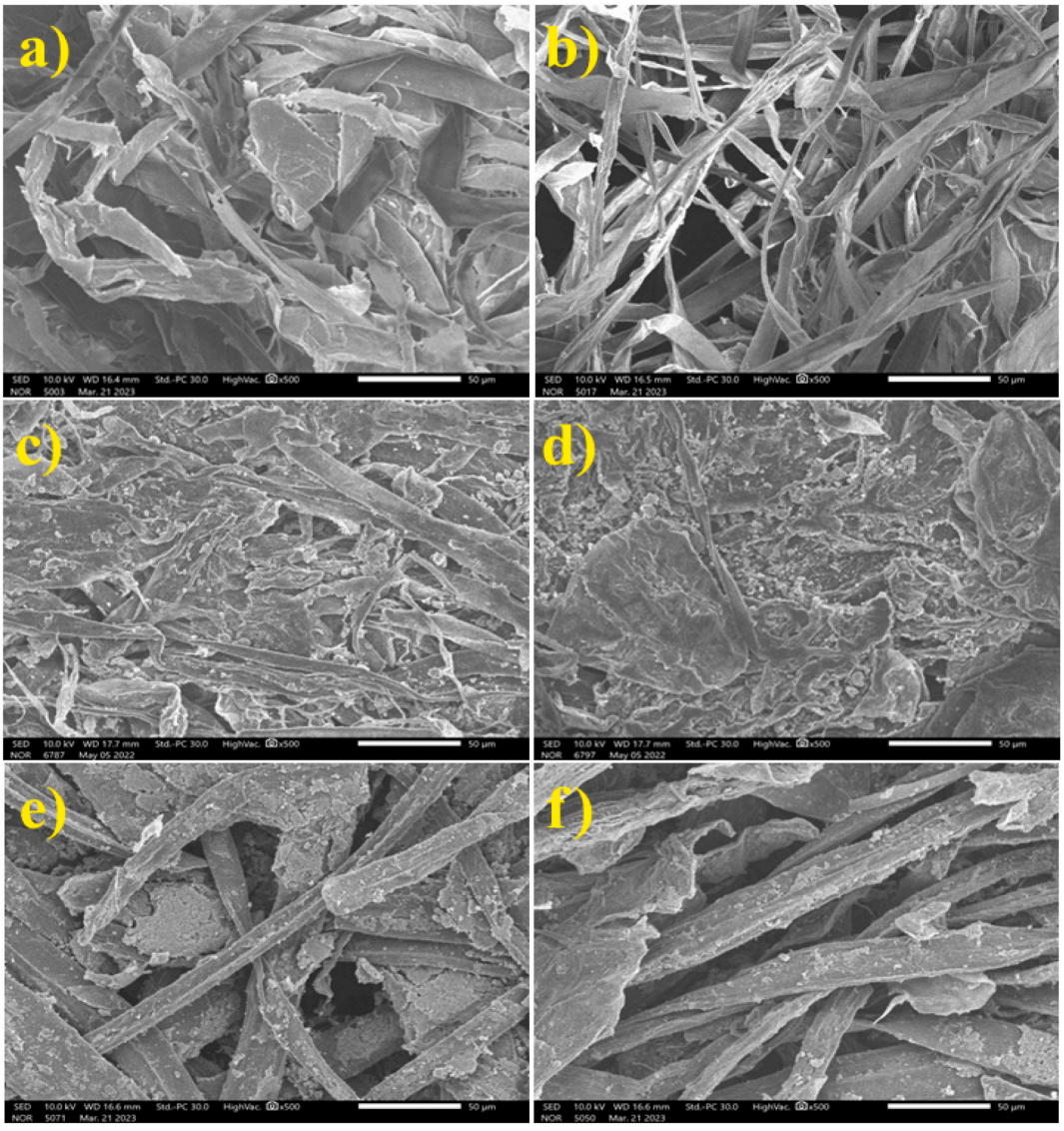

Fig. 6. SEM images of samples; a) CA-P, b) CA-K, c) Fe_3O_4-3@CA-KV, d) Fe_3O_4-3@CA-PV, e) Fe_3O_4-3@CA-KF and f) Fe_3O_4-3@CA-PF

absorbed [55]. In addition, the observed signals at 1098 and 898 cm^{-1} can be attributed to the symmetrical oscillations of C–O–C in pristine cellulose, indicating the presence of β-glycosidic bonds connecting glucose units [56]. The presence of two additional peaks at 1431 and 1231 cm^{-1} could potentially be attributed to the oscillation of the C–O bond in hemicellulose and the oscillation of the aromatic ring in lignin, as suggested by previous studies [57,58]. Following the application of chemical pretreatment, the peaks observed at 1736, 1430 and 1230 cm^{-1}, which are attributed to lignin and hemicellulose, were entirely absent from the FTIR spectrum. This absence serves as a clear indication of the substantial efficiency achieved in the removal process [59].

Scanning electron micrographs were utilized to observe the surface morphology of CA samples cross-linked with kymene and a mixture of PVA and GA, both before and after being doped with Fe_3O_4 NPs (Fig. 6). The investigation revealed an interconnected three-dimensional matrix with a great deal of branching and an abundance of porous structure in the inner section, and the structure of the CA material that was generated is more orderly organised and homogeneous and has a high porosity after being cross-linked by kymene and PVA-GA system (Fig. 6c–f). In addition, the results shown in Fig. 6a and b confirm that CA with kymene as cross-linker has a higher porosity than that of PVA-GA mixture. Fig. 6c–f exhibit the presence of diminutive Fe_3O_4 NPs, displaying a relatively homogeneous dispersion across the material's surface. Huixia Zhu et al. similarly showed comparable scanning electron microscopy (SEM) findings for Fe_3O_4@BC materials [60].

The composition of the synthesized samples, meanwhile, was ascertained via EDS and mapping techniques (Fig. 7). Fig. 7a–d shows that all Fe_3O_4@CA catalysts involved Fe, O and C elements, and the EDS results of all samples indicated no statistically significant difference between the actual results and calculated values (Table S2). The observed outcome can be attributed to the significant porosity exhibited by the aerogel samples, facilitating the efficient loading of Fe_3O_4 NPs onto their surfaces [61]. The CA samples from

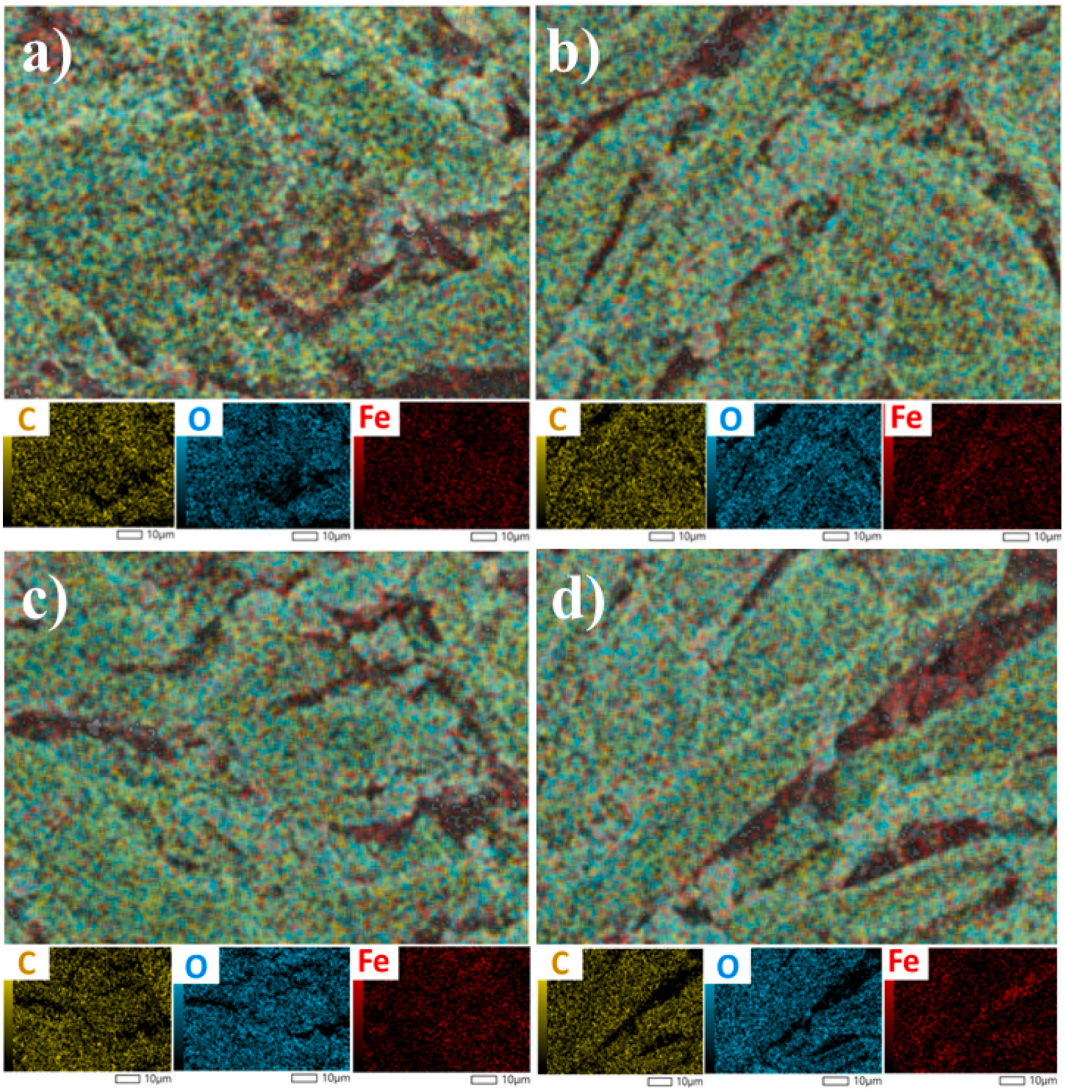

Fig. 7. EDS mapping of elements of samples; a) Fe_3O_4-3@CA-KV, b) Fe_3O_4@CA-PV, c) Fe_3O_4-3@CA-KF and d) Fe_3O_4@CA-PF.

WH in this study had a high porosity (98.2 %), which is comparable to the results obtained from a previous study concerning aerogels [11]. On the surface of the catalyst, the distribution of Fe and O was rather uniform during synthesis. The Fe_3O_4 NPs were effectively produced and incorporated into the surfaces of cellulose fibres.

TEM analysis (Fig. 8a) was used to investigate the microstructural characteristics of Fe_3O_4-3@CA-KF samples containing dark-field represented Fe_3O_4 NPs. By utilizing ImageJ software, the size distribution of Fe_3O_4 NPs extracted from TEM images was ascertained to be 5–15 nm for the spherical NPs (Fig. 8b). This result was entirely consistent with the XRD finding and SEM image of the material.

Fig. 9a and b illustrate the N_2 adsorption-desorption plots and BJH pore size distribution plots of the Fe_3O_4@CA hybrid aerogels fabricated using various methodologies. All the as-prepared samples' physical parameters, including specific surface areas, pore diameters and pore volumes, were calculated through BET and BJH analyses. The N_2 adsorption-desorption data presented in Fig. 9a demonstrates that the samples synthesized in this study display a type IV isotherm, as classified by the IUPAC. The pore size distribution plot (Fig. 9b) of the BJH analysis revealed that the majority of pores were distributed within the mesoporous range of 15–60 Å, with an average pore diameter of 26.6 Å. Additionally, the BET surface area and total pore volume decreased in the following order: Fe_3O_4-3@CA-KF (42.9 m^2/g, 0.113 cm^3/g) > Fe_3O_4@CA-PF (41.2 m^2/g, 0.100 cm^3/g) > Fe_3O_4-3@CA-KV (40.4 m^2/g, 0.083 cm^3/g) > Fe_3O_4@CA-PV (21.4 m^2/g, 0.113 cm^3/g). The sample with kymene as the cross-linker was superior to the PVA-GA system in terms of results. In addition, freeze drying strengthened the structure of the material, enhancing PNP degradation activity.

Fig. 9c and d shows that the PZC value and VSM curve of the samples had negligible differences. The PZC values of the samples fluctuated in a range of 6.55–6.70 in Fe_3O_4-3@CA-KF (6.55), Fe_3O_4@CA-PF (6.70), Fe_3O_4-3@CA-KV (6.66) and Fe_3O_4@CA-PV (6.63). The superparamagnetic nature of all Fe_3O_4@CA composites was evident from the magnetic hysteresis loops shown in Fig. 9d. The composites displayed zero remanence and coercivity [62]. The magnetisation saturation values of the Fe_3O_4@CA samples ranged from 20 emu/g to 30 emu/g. Besides, the Fe_3O_4@CA composites possess superparamagnetic and robust magnetic characteristics, which facilitate their separation from aqueous solutions in the presence of an external magnetic field. These results showed that the drying process and method only affect surface structure measurements, including specific surface area, pore diameter and pore volume, and do not considerably affect the magnetic properties and surface charge of Fe_3O_4-3@CA materials possibly because of the approximately equal Fe_3O_4 content.

3.3. Recyclability

The reusability of Fe_3O_4-3@CA-KF sample was tested (Fig. 10a). The Fenton reaction system can sustain approximately 80 % of PNP degradation rates throughout all five degradation phases, indicating that Fe_3O_4-3@CA-KF is highly recyclable and Fe_3O_4-3@CA-KF has excellent reusability. In addition, the Fe_3O_4-3@CA-KF composite was characterised by XRD, EDS and TEM after five cycles (Fig. 10b–d). There was no discernible alteration in the diffraction pattern of the Fe_3O_4 NPs, suggesting that the crystal structure of the catalyst remained unchanged after the treatment of PNP. In addition, the utilization of EDS mapping and mass percent elemental composition analysis (as depicted in Fig. 10b) indicated that there was no discernible disparity of statistical significance between the acquired data prior to and subsequent to the reaction. After five cycles of reuse, the composition and extensive dispersion of Fe_3O_4 NPs on the CA surface had a substantial impact on the activity of the catalyst. This finding implies that employing straightforward synthetic magnetic nanoparticles adorned with CA could serve as a viable approach to degrade PNP efficiently. Moreover, Fe_3O_4@CA catalysts are reusable following numerous reactions, satisfying the sustainable criteria. In contrast to previously reported magnetic catalysts, the present composite was synthesized by using a straightforward approach that is economically advantageous and exhibits remarkable performance and catalytic activity. Besides, F_3O_4 NPs can adhere to CA fibres, hence facilitating the straightforward retrieval and subsequent reuse of the catalyst through conventional filtering techniques.

4. Conclusion

Several approaches were used to fabricate of Fe_3O_4@CA catalytic samples, whereby the kymene and PVA-GA system were utilized

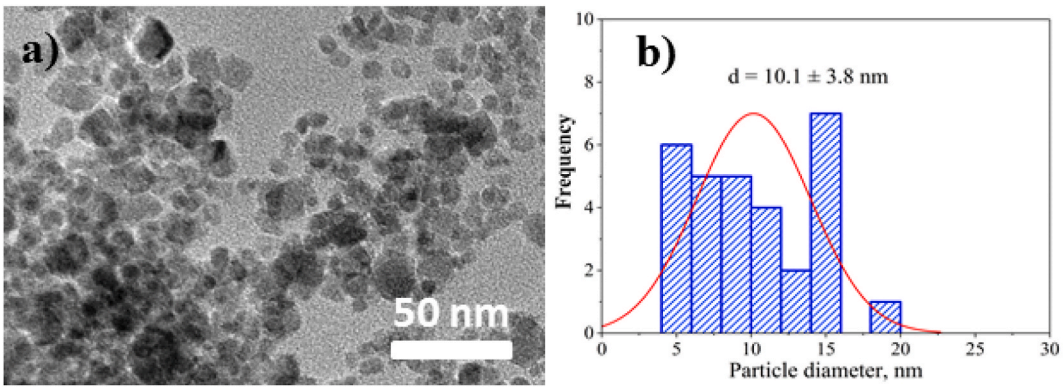

Fig. 8. The size distribution histogram (b) and TEM image (a) of magnetite nanoparticles adorning the Fe_3O_4-3@CA-KF sample.

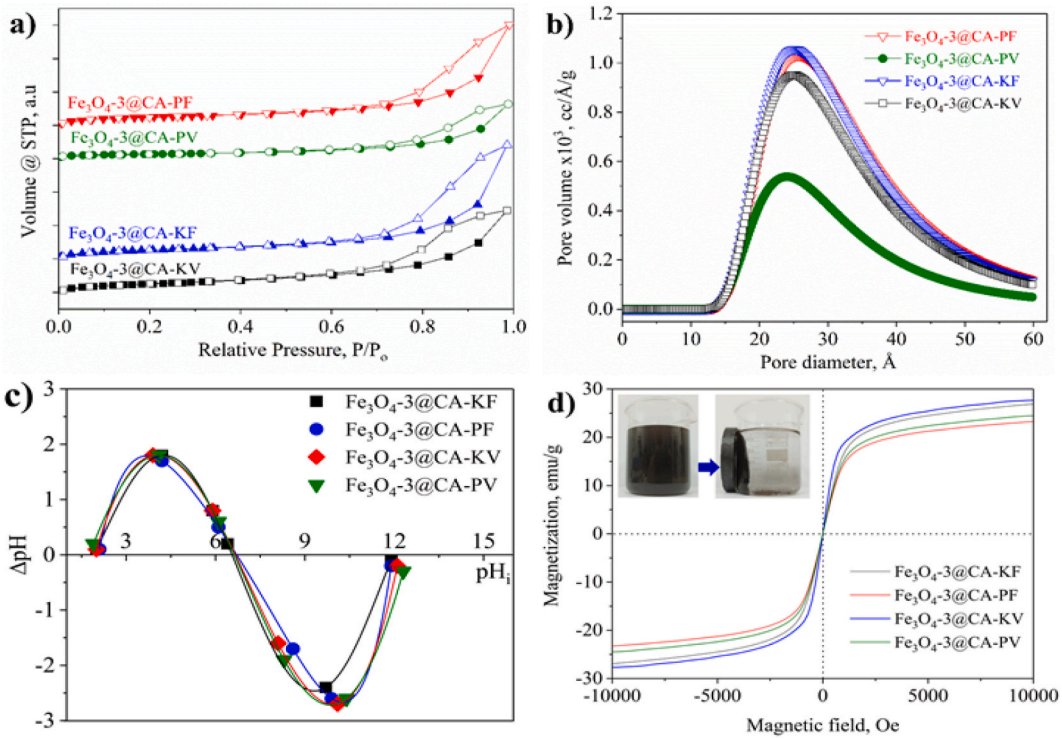

Fig. 9. N_2 adsorption/desorption isotherms (a), the BJH pore diameter distribution (b), point of zero charge (c) and VSM curve (d) of samples.

as cross-linking agents. The influences of heat drying and sublimation drying techniques on the PNP treatment procedure were investigated. The experiment analysis revealed that the most active catalysts were the Fe_3O_4 NPs decorated on CA with kymene as a cross-linker and the synthetic sample freeze-dried twice. The sample Fe_3O_4-3@CA-KF catalyst was confirmed as the best material under the optimal conditions (H_2O_2 dosage of 5.0 g/L, pH 3, and the amount used of the Fe_3O_4 catalyst with a content of 0.4 g/g CA) after 100 min of reaction in the Fenton system. The degradation rate of PNP at a high concentration of 2000 ppm was 92.5 %. Furthermore, it is worth noting that Fe_3O_4@CA exhibited a sustained and noteworthy level of catalytic efficiency in the Fenton degradation process of PNP, even after undergoing five successive iterations. This observation highlights the favourable reusability of Fe_3O_4@CA, a crucial aspect to consider for its practical implementation in various applications. In addition, the magnetic properties of Fe_3O_4@CA were advantageous in enabling the efficient separation and subsequent reuse of Fe_3O_4@CA from wastewater. Consequently, this finding will renew interest in future dyestuff remediation strategies based on stable and robust catalytic activity in repetitive reaction cycles and straightforward, inexpensive, and environmentally friendly synthesis procedures.

Funding statement

We acknowledge the support of time and facilities from Ho Chi Minh University of Technology (HCMUT), VNU-HCM for this study.

Data availability statement

Data included in article/supplementary material/referenced in article.

Additional information

No additional information is available for this paper.

CRediT authorship contribution statement

Thi Thuy Van Nguyen: Writing – original draft, Visualization, Validation, Resources, Methodology, Investigation, Formal analysis, Data curation, Conceptualization. **Quang Khai Nguyen:** Software, Resources, Methodology, Investigation, Formal analysis. **Ngoc Quan Thieu:** Software, Resources, Methodology, Investigation, Formal analysis. **Hoang Diem Trinh Nguyen:** Writing – original draft, Visualization, Validation, Resources, Methodology, Investigation, Formal analysis, Data curation, Conceptualization. **Thanh Gia Thien Ho:** Writing – original draft, Visualization, Validation, Resources, Methodology, Investigation, Formal analysis, Data curation,

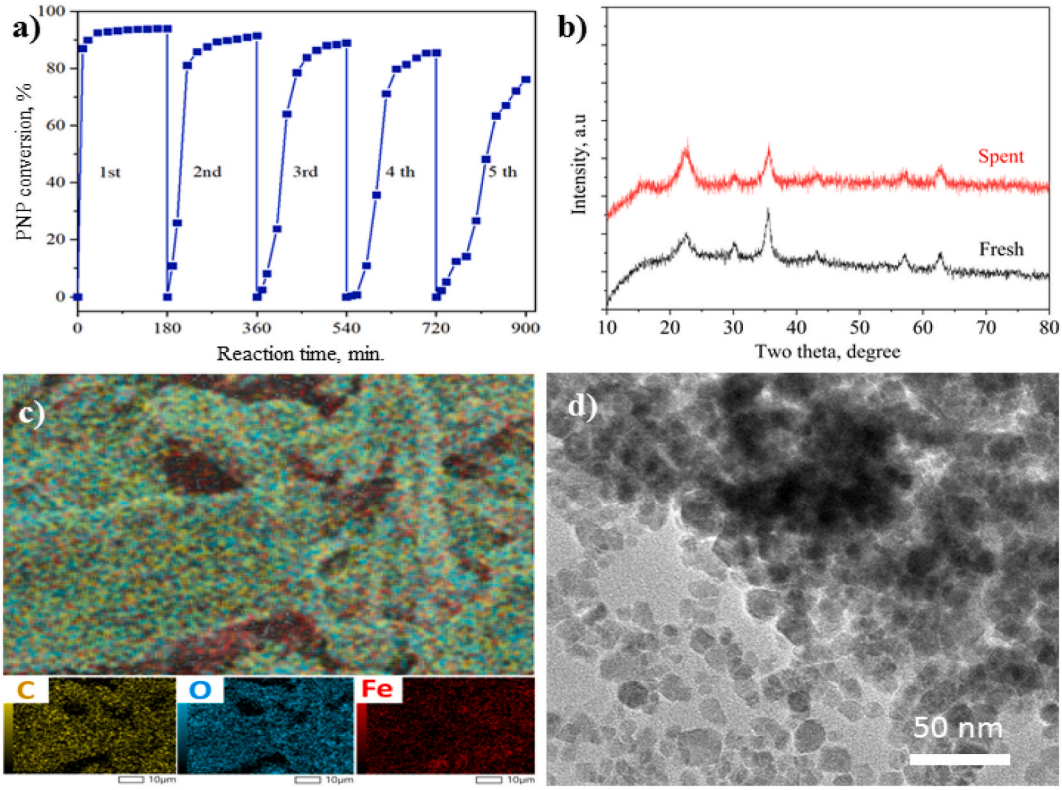

Fig. 10. Catalytic stability of the Fe_3O_4-3@CA-KF sample in the heterogeneous Fenton degradation of PNP over five consecutive cycles (a); the comparison of fresh and spent XRD patterns Fe_3O_4-3@CA-KF samples (b) and elemental mapping (c) and TEM image of spent Fe_3O_4-3@CA-KF sample.

Conceptualization. **Ba Long Do:** Software, Resources, Methodology, Investigation, Formal analysis. **Thi Thuy Phuong Pham:** Software, Resources, Methodology, Investigation, Formal analysis. **Tri Nguyen:** Writing – review & editing, Visualization, Validation, Supervision, Methodology, Investigation, Data curation, Conceptualization. **Huynh Ky Phuong Ha:** Writing – review & editing, Visualization, Validation, Supervision, Methodology, Investigation, Data curation, Conceptualization.

Declaration of competing interest

The authors declare that they have no known competing financial interests or personal relationships that could have appeared to influence the work reported in this paper.

Appendix A. Supplementary data

Supplementary data to this article can be found online at https://doi.org/10.1016/j.heliyon.2023.e22319.

References

[1] S. Ahankari, P. Paliwal, A. Subhedar, H. Kargarzadeh, Recent developments in nanocellulose-based aerogels in thermal applications: a review, ACS Nano 15 (2021) 3849–3874.
[2] D. Shen, J. Liu, L. Gan, N. Huang, M. Long, Green synthesis of Fe_3O_4/cellulose/polyvinyl alcohol hybride aerogel and its application for dye removal, J. Polym. Environ. 26 (2018) 2234–2242.
[3] J.P. de Oliveira, G.P. Bruni, S.L.M. El Halal, F.C. Bertoldi, A.R.G. Dias, E. da Rosa Zavareze, Cellulose nanocrystals from rice and oat husks and their application in aerogels for food packaging, Int. J. Biol. Macromol. 124 (2019) 175–184.
[4] A.K. Das, M.N. Islam, R.K. Ghosh, R. Maryana, Cellulose-based bionanocomposites in energy storage applications-A review, Heliyon 9 (2023), e13028.
[5] N. Rong, C. Chen, K. Ouyang, K. Zhang, X. Wang, Z. Xu, Adsorption characteristics of directional cellulose nanofiber/chitosan/montmorillonite aerogel as adsorbent for wastewater treatment, Sep. Purif. Technol. 274 (2021), 119120.
[6] T. Hoshi, K. Yamazaki, Y. Sato, T. Shida, T. Aoyagi, Production of hollow-type spherical bacterial cellulose as a controlled release device by newly designed floating cultivation, Heliyon 4 (2018), e00873.

[7] E.B. Yahya, M.M. Alzalouk, K.A. Alfallous, A.F. Abogmaza, Antibacterial cellulose-based aerogels for wound healing application: a review, Biomed. Res. Ther. 7 (2020) 4032–4040.

[8] X. Chen, X. Xu, W. Li, B. Sun, J. Yan, C. Chen, J. Liu, J. Qian, D. Sun, Effective drug carrier based on polyethylenimine-functionalized bacterial cellulose with controllable release properties, ACS Appl. Bio Mater. 1 (2018) 42–50.

[9] T.T.V. Nguyen, N. Tri, B.A. Tran, T. Dao Duy, S.T. Nguyen, T.-A. Nguyen, A.N. Phan, P. Mai Thanh, H.K.P. Huynh, Synthesis, characteristics, oil adsorption, and thermal insulation performance of cellulosic aerogel derived from water hyacinth, ACS Omega 6 (2021) 26130–26139.

[10] T.T. Van Nguyen, G.X. Yang, A.N. Phan, T. Nguyen, T.G.-T. Ho, S.T. Nguyen, H.H.K. Phuong, Insights into the effects of synthesis techniques and crosslinking agents on the characteristics of cellulosic aerogels from Water Hyacinth, RSC Adv. 12 (2022) 19225–19231.

[11] L.N. Phat, T.Q. Thang, H.C. Nguyen, D.T.M. Duyen, D.X. Tien, B.D.D. Khoa, P.T. Khang, N.T.H. Giang, H.M. Nam, M.T. Phong, Fabrication and modification of cellulose aerogels from Vietnamese water hyacinth for oil adsorption application, Korean J. Chem. Eng. 38 (2021) 2247–2255.

[12] H. Wang, X. Yuan, G. Zeng, Y. Wu, Y. Liu, Q. Jiang, S. Gu, Three dimensional graphene based materials: synthesis and applications from energy storage and conversion to electrochemical sensor and environmental remediation, Adv. Colloid Interface Sci. 221 (2015) 41–59.

[13] F. Rechberger, M. Niederberger, Synthesis of aerogels: from molecular routes to 3-dimensional nanoparticle assembly, Nanoscale Horiz 2 (2017) 6–30.

[14] C. Ruan, Y. Ma, G. Shi, C. He, C. Du, X. Jin, X. Liu, S. He, Y. Huang, Self-assembly cellulose nanocrystals/SiO_2 composite aerogel under freeze-drying: adsorption towards dye contaminant, Appl. Surf. Sci. 592 (2022), 153280.

[15] M. Li, J. Qiu, J. Xu, J. Yao, Cellulose/TiO_2-based carbonaceous composite film and aerogel for highly efficient photocatalysis under visible light, Ind. Eng. Chem. Res. 59 (2020) 13997–14003.

[16] R.T. Olsson, M. Azizi Samir, G. Salazar-Alvarez, L. Belova, V. Ström, L.A. Berglund, O. Ikkala, J. Nogues, U.W. Gedde, Making flexible magnetic aerogels and stiff magnetic nanopaper using cellulose nanofibrils as templates, Nat. Nanotechnol. 5 (2010) 584–588.

[17] K.Y. Chong, C.H. Chia, S. Zakaria, M.S. Sajab, S.W. Chook, P.S. Khiew, $CaCO_3$-decorated cellulose aerogel for removal of Congo Red from aqueous solution, Cellulose 22 (2015) 2683–2691.

[18] H. Jin, M. Kettunen, A. Laiho, H. Pynnonen, J. Paltakari, A. Marmur, O. Ikkala, R.H. Ras, Superhydrophobic and superoleophobic nanocellulose aerogel membranes as bioinspired cargo carriers on water and oil, Langmuir 27 (2011) 1930–1934.

[19] A. Javadi, Q. Zheng, F. Payen, A. Javadi, Y. Altin, Z. Cai, R. Sabo, S. Gong, Polyvinyl alcohol-cellulose nanofibrils-graphene oxide hybrid organic aerogels, ACS Appl. Mater. Interfaces 5 (2013) 5969–5975.

[20] J. Feng, S.T. Nguyen, Z. Fan, H.M. Duong, Advanced fabrication and oil absorption properties of super-hydrophobic recycled cellulose aerogels, Chem. Eng. J. 270 (2015) 168–175.

[21] D.K. Le, G.N. Ng, H.W. Koh, X. Zhang, Q.B. Thai, N. Phan-Thien, H.M. Duong, Methyltrimethoxysilane-coated recycled polyethylene terephthalate aerogels for oil spill cleaning applications, Mater. Chem. Phys. 239 (2020), 122064.

[22] J.-L. Zhu, S.-P. Chen, G.-Q. Ma, J.-X. Ren, H.-L. Li, W. Lin, H.-D. Huang, Z.-M. Li, Regenerated cellulose as template for in-situ synthesis of monoclinic titanium dioxide nanocomposite carbon aerogel towards multiple application in water treatment, J. Colloid Interface Sci. 630 (2023) 772–782.

[23] C. Jiménez-Saelices, B. Seantier, B. Cathala, Y. Grohens, Effect of freeze-drying parameters on the microstructure and thermal insulating properties of nanofibrillated cellulose aerogels, J. Sol. Gel Sci. Technol. 84 (2017) 475–485.

[24] Y. Jiao, C. Wan, W. Bao, H. Gao, D. Liang, J. Li, Facile hydrothermal synthesis of Fe_3O_4@ cellulose aerogel nanocomposite and its application in Fenton-like degradation of Rhodamine B, Carbohydr. Polym. 189 (2018) 371–378.

[25] N.T.T. Van, A.N. Phan, V.C. Cuong, N.T.T. Van, H.G.-T. Thanh, N.Q. Khai, N. Tri, T.-T. Nguyen, X.-T. Bui, K.P.H. Huynh, Enhanced heterogeneous Fenton degradation of p-nitrophenol by Fe_3O_4 nanoparticles decorated cellulose aerogel from banana stem, Environ. Technol. Innov. (2023), 103041.

[26] X. Zhu, L. Zhang, G. Zou, Q. Chen, Y. Guo, S. Liang, L. Hu, M. North, H. Xie, Carboxylcellulose hydrogel confined-Fe_3O_4 nanoparticles catalyst for Fenton-like degradation of Rhodamine B, Int. J. Biol. Macromol. 180 (2021) 792–803.

[27] M.S. Sajab, C.H. Chia, C.H. Chan, S. Zakaria, H. Kaco, S.W. Chook, S.X. Chin, Bifunctional graphene oxide–cellulose nanofibril aerogel loaded with Fe (III) for the removal of cationic dye via simultaneous adsorption and Fenton oxidation, RSC Adv. 6 (2016) 19819–19825.

[28] J. Mehralipour, S. Bagheri, M. Gholami, Synthesis and characterization of rGO/Fe^0/Fe_3O_4/TiO_2 nanocomposite and application of photocatalytic process in the decomposition of penicillin G from aqueous, Heliyon 9 (2023), e18172.

[29] H. Niu, Y. Zheng, S. Wang, L. Zhao, S. Yang, Y. Cai, Continuous generation of hydroxyl radicals for highly efficient elimination of chlorophenols and phenols catalyzed by heterogeneous Fenton-like catalysts yolk/shell Pd@Fe_3O_4@metal organic frameworks, J. Hazard Mater. 346 (2018) 174–183.

[30] N.A. Zubir, C. Yacou, J. Motuzas, X. Zhang, J.C. Diniz da Costa, Structural and functional investigation of graphene oxide–Fe_3O_4 nanocomposites for the heterogeneous Fenton-like reaction, Sci. Rep. 4 (2014) 4594.

[31] E.N. Bakatula, D. Richard, C.M. Neculita, G.J. Zagury, Determination of point of zero charge of natural organic materials, Environ. Sci. Pollut. Res. 25 (2018) 7823–7833.

[32] B. Neppolian, J.-S. Park, H. Choi, Effect of Fenton-like oxidation on enhanced oxidative degradation of para-chlorobenzoic acid by ultrasonic irradiation, Ultrason. Sonochem. 11 (2004) 273–279.

[33] C. Zaharia, D. Suteu, A. Muresan, R. Muresan, A. Popescu, Textile wastewater treatment by homogenous oxidation with hydrogen peroxide, Environ. Eng. Manag. J. 8 (2009) 1359–1369.

[34] A. Gangwar, A. Singh, S. Pal, I. Sinha, S.S. Meena, N.K. Prasad, Magnetic nanocomposites of Fe_3C or Ni-substituted (Fe_3C/Fe_3O_4) with carbon for degradation of methylene orange and p-nitrophenol, J. Clean. Prod. 309 (2021), 127372.

[35] H. Ren, Y. Su, X. Han, R. Zhou, Synthesis and characterization of saponin-modified Fe_3O_4 nanoparticles as heterogeneous Fenton-catalyst with enhanced degradation of p-nitrophenol, J. Chem. Technol. Biotechnol. 92 (2017) 1421–1427.

[36] X. Tang, Z. Li, K. Liu, X. Luo, D. He, M. Ao, Q. Peng, Sulfidation modified Fe_3O_4 nanoparticles as an efficient Fenton-like catalyst for azo dyes degradation at wide pH range, Powder Technol. 376 (2020) 42–51.

[37] A.-R.A. Giwa, I.A. Bello, A.B. Olabintan, O.S. Bello, T.A. Saleh, Kinetic and thermodynamic studies of fenton oxidative decolorization of methylene blue, Heliyon 6 (2020), e04454.

[38] X. Tian, Y. Liu, W. Chi, Y. Wang, X. Yue, Q. Huang, C. Yu, Catalytic degradation of phenol and p-nitrophenol using Fe_3O_4/MWCNT nanocomposites as heterogeneous Fenton-like catalyst, Water Air Soil Pollut. 228 (2017) 1–12.

[39] Y. Segura, F. Martínez, J.A. Melero, R. Molina, R. Chand, D.H. Bremner, Enhancement of the advanced Fenton process (Fe^0/H_2O_2) by ultrasound for the mineralization of phenol, Appl. Catal. B Environ. 113 (2012) 100–106.

[40] S. Yu, J. Hu, J. Wang, Gamma radiation-induced degradation of p-nitrophenol (PNP) in the presence of hydrogen peroxide (H_2O_2) in aqueous solution, J. Hazard Mater. 177 (2010) 1061–1067.

[41] W. Luo, L. Zhu, N. Wang, H. Tang, M. Cao, Y. She, Efficient removal of organic pollutants with magnetic nanoscaled $BiFeO_3$ as a reusable heterogeneous Fenton-like catalyst, Environ. Sci. Technol. 44 (2010) 1786–1791.

[42] X. Hu, B. Liu, Y. Deng, H. Chen, S. Luo, C. Sun, P. Yang, S. Yang, Adsorption and heterogeneous Fenton degradation of 17α-methyltestosterone on nano Fe_3O_4/MWCNTs in aqueous solution, Appl. Catal. B Environ. 107 (2011) 274–283.

[43] W. Pan, G. Zhang, T. Zheng, P. Wang, Degradation of p-nitrophenol using CuO/Al_2O_3 as a Fenton-like catalyst under microwave irradiation, RSC Adv. 5 (2015) 27043–27051.

[44] Y. Dang, Y. Bai, Y. Zhang, X. Yang, X. Sun, S. Yu, Y. Zhou, Tannic acid reinforced electro-Fenton system based on GO-Fe_3O_4/NF cathode for the efficient catalytic degradation of PNP, Chemosphere 289 (2022), 133046.

[45] H. Nguyen, H.K.P. Ha, S.T. Nguyen, T.T. Van Nguyen, A.T. Nguyen, A. Phan, Insights into sustainable aerogels from lignocellulosic materials, J. Mater. Chem. A 10 (2022) 23467–23482.

[46] X. Zhu, L. Zhang, G. Zou, Q. Chen, Y. Guo, S. Liang, L. Hu, M. North, H. Xie, Carboxylcellulose hydrogel confined-Fe3O4 nanoparticles catalyst for Fenton-like degradation of Rhodamine B, Int. J. Biol. Macromol. 180 (2021) 792–803.

[47] A. Bashir, A.H. Pandith, A. Qureashi, L.A. Malik, M. Gani, J.M. Perez, Catalytic propensity of biochar decorated with core-shell nZVI@ Fe3O4: a sustainable photo-Fenton catalysis of methylene blue dye and reduction of 4-nitrophenol, J. Environ. Chem. Eng. 10 (2022), 107401.
[48] S. Shaker, S. Zafarian, C. Chakra, K. Rao, Preparation and characterization of magnetite nanoparticles by sol-gel method for water treatment, Int. J. Innov. Res. Sci. Eng. 2 (2013) 2969–2973.
[49] A.A. Mohammed, S.S. Isra'a, Bentonite coated with magnetite Fe_3O_4 nanoparticles as a novel adsorbent for copper (II) ions removal from water/wastewater, Environ. Technol. Innov. 10 (2018) 162–174.
[50] F. Abdelghaffar, Biosorption of anionic dye using nanocomposite derived from chitosan and silver Nanoparticles synthesized via cellulosic banana peel bio-waste, Environ. Technol. Innov. 24 (2021), 101852.
[51] X. Sun, C. Zheng, F. Zhang, Y. Yang, G. Wu, A. Yu, N. Guan, Size-controlled synthesis of magnetite (Fe_3O_4) nanoparticles coated with glucose and gluconic acid from a single Fe (III) precursor by a sucrose bifunctional hydrothermal method, J. Phys. Chem. C 113 (2009) 16002–16008.
[52] M. Gopiraman, D. Deng, S. Saravanamoorthy, I.-M. Chung, I.S. Kim, Gold, silver and nickel nanoparticle anchored cellulose nanofiber composites as highly active catalysts for the rapid and selective reduction of nitrophenols in water, RSC Adv. 8 (2018) 3014–3023.
[53] J. Jiang, J. Zou, L. Zhu, L. Huang, H. Jiang, Y. Zhang, Degradation of methylene blue with H_2O_2 activated by peroxidase-like Fe_3O_4 magnetic nanoparticles, J. Nanosci. Nanotechnol. 11 (2011) 4793–4799.
[54] H. Hu, Z. Wang, L. Pan, S. Zhao, S. Zhu, Ag-coated Fe_3O_4@SiO_2 three-ply composite microspheres: synthesis, characterization, and application in detecting melamine with their surface-enhanced Raman scattering, J. Phys. Chem. C 114 (2010) 7738–7742.
[55] E. Fortunati, D. Puglia, F. Luzi, C. Santulli, J.M. Kenny, L. Torre, Binary PVA bio-nanocomposites containing cellulose nanocrystals extracted from different natural sources: Part I, Carbohydr. Polym. 97 (2013) 825–836.
[56] S. Williams, C.L. Okolie, J. Deshmukh, L. Hawco, J. McNeil, A.C. Nganou Assonkeng, C. Bennett, M. Mkandawire, Magnetizing cellulose fibers with $CoFe_2O_4$ nanoparticles for smart wound dressing for healing monitoring capability, ACS Appl. Bio Mater. 2 (2019) 5653–5662.
[57] A. Boukir, S. Fellak, P. Doumenq, Structural characterization of Argania spinosa Moroccan wooden artifacts during natural degradation progress using infrared spectroscopy (ATR-FTIR) and X-Ray diffraction (XRD), Heliyon 5 (2019), e02477.
[58] A. Parihar, J. Vongsvivut, S. Bhattacharya, Synchrotron-based infra-red spectroscopic insights on thermo-catalytic conversion of cellulosic feedstock to levoglucosenone and furans, ACS Omega 4 (2019) 8747–8757.
[59] J. Xie, Preparation of Cellulose Nanofibers from Bamboo Using Microwave Liquefaction, Louisiana State University and Agricultural & Mechanical College, 2018.
[60] H. Zhu, S. Jia, T. Wan, Y. Jia, H. Yang, J. Li, L. Yan, C. Zhong, Biosynthesis of spherical Fe_3O_4/bacterial cellulose nanocomposites as adsorbents for heavy metal ions, Carbohydr. Polym. 86 (2011) 1558–1564.
[61] J. Dasgupta, S. Chakraborty, J. Sikder, R. Kumar, D. Pal, S. Curcio, E. Drioli, The effects of thermally stable titanium silicon oxide nanoparticles on structure and performance of cellulose acetate ultrafiltration membranes, Sep. Purif. Technol. 133 (2014) 55–68.
[62] R. Yang, Q. Peng, B. Yu, Y. Shen, H. Cong, Yolk-shell Fe_3O_4@MOF-5 nanocomposites as a heterogeneous Fenton-like catalyst for organic dye removal, Sep. Purif. Technol. 267 (2021), 118620.